JOURNAL OF PROPULSION AND POWER
Vol. 22, No. 5, September–October 2006

Thermal Analysis of a Lithium Vaporizer for a High-Power Magnetoplasmadynamic Thruster

B. St. Rock* and J. J. Blandino†
Worcester Polytechnic Institute, Worcester, Massachusetts 021609
and
K. R. Anderson‡ and J. E. Polk§
NASA Jet Propulsion Laboratory, Pasadena, California 91109

DOI: 10.2514/1.19773

The lithium vaporizer for a high-power magnetoplasmadynamic thruster is modeled using a 1-D, thermal-resistive network. We use this model to calculate the required vaporizer length and power as a function of mass flow rate, channel geometry, and material properties. After comparing results predicted by this model with preheat power data for a 200 kW thruster, we investigate performance over a parameter space of interest for the Advanced Lithium-Fed Appled-Field Lorentz Force Accelerator thruster. Heater power sensitivity to cathode tube emissivity, mass flow rate, and vapor superheat are presented. The cold-start heater power for 80 mg/s is found to range from 3.38 to 3.60 kW, corresponding to a vaporizer (axial) length of 18 to 26 cm. The strongest drivers of vaporizer performance are cathode tube emissivity and the conduction heat flow path through the mounting flange. Also, for the baseline case, it is shown that increasing the vapor superheat from 100 to 300 K has the effect of lowering the vaporizer thermal efficiency from 57 to 49%. Finally, the network model results are used to provide boundary conditions for a finite-element thermal model of the cathode assembly. This model is used to calculate a higher resolution temperature distribution throughout the cathode assembly.

Nomenclature

a	=	channel depth, m
b	=	cross-sectional channel width, m
b'	=	actual channel width, m
c	=	cross-sectional channel spacing, m
c'	=	actual channel spacing, m
D_h	=	hydraulic diameter, m
E	=	two-phase correlation parameter
F	=	radiation view factor, dimensionless
F_1	=	empirical coefficient, dimensionless
F_2	=	empirical coefficient, dimensionless
G	=	mass flux, kg m^{-2} s^{-1}
h_f	=	heat transfer coefficient, W/m^{2}K
h_{fg}	=	latent heat of vaporization, J/kg
k	=	thermal conductivity, W/m-K
L_{NC}	=	length of vaporizer with no channels, m
L_P	=	length of pooled, liquid annulus inlet region, m
$\dot{m}$	=	mass flow rate, kg/s
Nu	=	Nusselt number, dimensionless
P	=	heater power, W
Pe	=	Peclet number, dimensionless
Pr	=	Prandtl number, dimensionless
p	=	thread pitch, m
q	=	network heat flow, W
R	=	network resistance, K/W
Re	=	Reynolds number, dimensionless
R''_C	=	thermal contact resistance, K-m^2/W
r	=	component radius, m
s	=	path coordinate, m
t	=	flange or wall thickness, m
T	=	nodal temperature, K
X	=	vapor mass fraction or quality, dimensionless
x	=	axial coordinate, m
X_{tt}	=	Martinelli parameter, dimensionless
α	=	void fraction, dimensionless
γ	=	two-phase correlation parameter
Δs	=	grid spacing, m
ΔT_{SH}	=	vapor superheat, K
μ_L	=	liquid dynamic viscosity, kg/ms
μ_V	=	vapor dynamic viscosity, kg/ms
ρ_L	=	liquid mass density, kg/m^3
ρ_V	=	vapor mass density, kg/m^3
σ	=	Stefan-Boltzmann constant, J K^{-4} m^{-2} s^{-1}
ϕ_L	=	empirical parameter, dimensionless

Subscripts

AN	=	anode
C	=	cathode assembly
CT	=	cathode tube
F	=	fluid
HF	=	heater flange
I	=	inner
MF	=	mounting flange
m	=	molybdenum
O	=	outer
R	=	radiation
S	=	heat sink
t	=	tungsten
VT	=	vaporizer tube

Presented at the 41st Joint Propulsion Conference and Exhibit, Tucson, AZ, 10–13 July 2005; received 30 August 2005; revision received 24 January 2006; accepted for publication 27 January 2006.

*Graduate Student, Mechanical Engineering Department. Student Member AIAA.
†Assistant Professor, Mechanical Engineering Department. Senior Member AIAA.
‡Associate Professor of Mechanical Engineering, California State Polytechnic University, Pomona.
§Senior Staff. Senior Member AIAA.

I. Introduction

A space-qualified solar or nuclear power source capable of producing several hundred kilowatts of electrical power enables a number of ambitious robotic exploration missions to the

outer planets and could also support human exploration of the moon and Mars. In addition to purely robotic missions, a high-power solar or nuclear system would enable the use of high performance electric propulsion systems for the transport of cargo to Mars ahead of a human crew.

The Jupiter Icy Moons Orbiter (JIMO) is a mission proposed to demonstrate technology for these high-power outer solar system missions. The propulsion system for JIMO has been proposed to include a combination of advanced gridded ion thrusters and high-power Hall thrusters. The combination of ion and Hall thrusters is needed to optimize the system performance which needs to balance high specific impulse (6000–8000 s) provided by the ion thrusters throughout most of the mission with the higher thrust needed for operations near Europa provided by the Hall thrusters [1]. The Herakles thrusters, with a power per thruster capability of 30 kW represent the state of the art in ion thruster technology and would be operated in clusters to process the 200 kW available for a JIMO mission [2].

More demanding missions are being proposed that will require hundreds of kilowatts to several megawatts. These missions include outer solar system robotic missions such as a Saturn Orbiter (with moon tour) with a ΔV of 33 km/sec and an interstellar precursor mission with a ΔV of 28–53 km/s [3]. These studies have considered power levels ranging from 250 kW to 2.75 MW. Even with the advanced Herakles technology, the number of thrusters needed to process such high power leads to increasingly complex and massive clusters of thrusters, feed system components, and power processors. One option which has been considered is the use of lithium-fueled magnetoplasmadynamic (MPD) thrusters or Lorentz force accelerators (LFA) which have demonstrated the capability to process from 200 to 500 kW for a single thruster in tests performed at the Moscow Aviation Institute (MAI) [3].

The MPD thruster is an electromagnetic thruster in which the plasma is accelerated through a Lorentz body force resulting from the interaction of the current and magnetic fields (both self-generated and applied). Choueiri [4] presents a thorough discussion of the acceleration mechanisms in these devices. MPD thrusters have been studied since the 1960s at numerous research laboratories. For an excellent summary of thruster performance data, the interested reader is referred to a review by Kodys and Choueiri [5]. While the focus of the present work is in devices using lithium propellant, the aforementioned reviews also include data for other propellants including hydrogen and argon. In fact, the ability of MPD devices to accelerate a variety of gases has also led to its consideration for terrestrial materials processing applications [6].

Figure 1 shows a simplified section view for one concept for the Advanced Lithium-Fed Appled-Field Lorentz Force Accelerator ($ALFA^2$). The basic elements are the cathode assembly, anode, solenoids, and heat pipes. The thruster will use a multichannel hollow cathode to sustain a steady-state discharge of several thousand amperes. The thruster incorporates a number of innovative features designed to improve efficiency and extend lifetime. The $ALFA^2$ thruster is being designed to target a nominal performance of 60 to 63% thruster efficiency at a specific impulse (Isp) value of 6200 s and a power level of 245 kW [3].

The efficient operation of $ALFA^2$ requires the reliable delivery of a controlled mass flow (tens of mg/s) of lithium vapor. A proof-of-concept version of the $ALFA^2$ thruster will be designed to operate in the 100–240 kW power range. This paper presents models and results intended to help understand the sensitivity of the vaporizer performance to several key design parameters. The insights gained from this analysis will guide the eventual design of a 500 kW thruster in support of robotic planetary exploration.

The lithium propellant, which has a melting point of approximately 180°C (453 K), will be delivered by the propellant feed system to the thruster in a liquid state. The liquid must then be vaporized before delivery to the multichannel hollow cathode in order to sustain an electrical discharge of several thousand amperes. For an efficient, compact thruster, the vaporizer is integrated into the cathode assembly. While the latent heat of vaporization will need to be provided by electrical heating for cold starts, a portion of this energy input will be provided during operation by heat from the discharge itself which is conducted into the vaporizer channels.

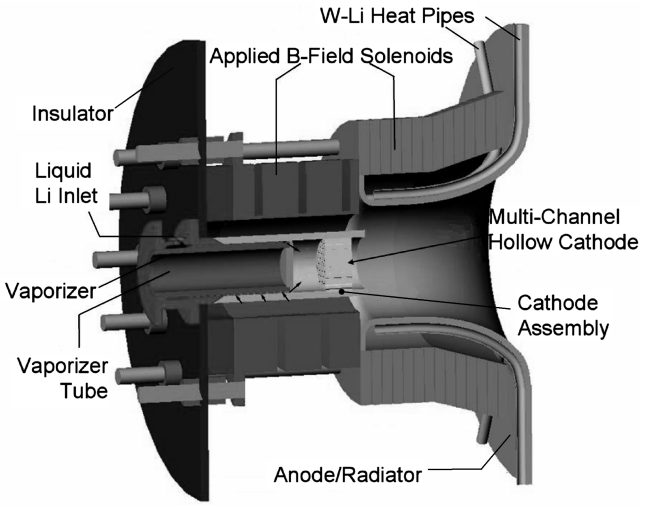

Fig. 1 Cutaway drawing of the conceptual $ALFA^2$ thruster showing major components.

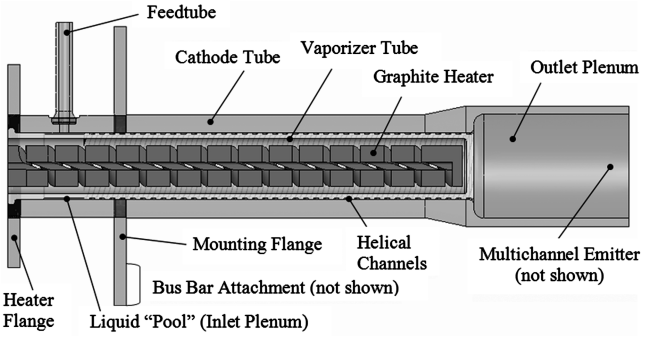

Fig. 2 Axial cutaway drawing of the cathode assembly showing all main components/features of the cathode assembly.

Minimizing the heat load required to sustain vaporization during operation requires a careful cathode-vaporizer design in which the heat from the arc is matched with the mass flow rate. In addition, conducted and radiated heat losses from the thruster body and arc must be considered in order to design the vaporizer for optimal thruster efficiency. The objective of the model presented in this paper is to provide a tool which can be used to quickly determine vaporizer performance sensitivity to mass flow rate, channel geometry, surface emissivity, number of channels (leads), and initial and final fluid thermodynamic states. In particular, we concentrate on the cold-start problem, during which an electric heater must provide all of the power required for full vaporization.

This paper is organized as follows. Section II presents a description of the network model, including the representative vaporizer geometry and thermal resistances used in the equation system. We also describe in detail the convection coefficient correlations used as these are crucial to the estimation of channel length and dryout point. Section III presents results of the network model. We begin by comparing the performance predicted by the model with some data available for a 200-kW MAI thruster [7]. Overall, the basic features of the cathode design for $ALFA^2$ are similar to the design of the MAI 200 kW thruster. Results are then provided showing the sensitivity of the vaporizer performance to cathode emissivity, mass flow rate, and vapor superheat. Section IV describes the finite-element thermal model (FETM) that was generated using IDEAS Thermal Modeling Group (TMG) software. The FETM uses the network model to provide input in terms of heat fluxes. A description of the governing equations employed by the IDEAS-TMG model, as well as the numerical accuracy of the software is the focus of Sec. V. In Sec. VI, we present the results of

this FETM applied to a candidate geometry for the ALFA^2 vaporizer and follow with conclusions in Sec. VII.

II. Network Model Description

A. Cathode Assembly

The lithium vaporizer for the ALFA^2 thruster is integrated into the cathode assembly. In Fig. 2, we show an axial cutaway of the cathode assembly, highlighting all of the main components and features. The vaporizer and cathode tube are made from tungsten, and both flanges are made from molybdenum. These materials are ideal for this application due to the high temperature operation of the cathode. The heater flange, along with isolator plates (not shown) are used to fix the graphite heater insert into the upstream end of the vaporizer. The mounting flange attaches the cathode assembly to a bus bar that will pass several thousand amperes into the cathode during operation. The vaporizer tube fits tightly inside the cathode tube, and has a helical groove engraved on its outer surface [can have multiple grooves (leads) to provide multiple fluid channels]. The channel for the fluid is created by the gaps between the vaporizer tube and cathode tube. Liquid lithium enters the vaporizer through the feed tube, into an inlet "pool" (or inlet plenum), and then into the helical channels. The liquid flows through the helical channels, becoming fully vaporized, then exits the vaporizer into the outlet plenum and through a multichannel emitter.

B. Description of the Network Model

The first-order network model uses a one-dimensional (radial) thermal resistance network to determine the temperature at several different radial locations between the vaporizer tube inner wall and the outer cathode tube wall. The model is divided into two parts, one for the portion of the vaporizer tube with the flow channels and one for the "prechannel" portion extending from the base end to the channel inlet. Figure 3 represents an axial cutaway of a portion of the vaporizer tube closest to the inlet. The inlet tube is not modeled explicitly, but the initial lithium temperature is taken to be a value representative of what it would be entering the tube (500 K). The vaporizer tube, cathode tube, and mounting flange radii are measured from the centerline indicated by the horizontal dotted line. The geometric variables shown in Fig. 3, along with the channel dimensions described later were selected to represent either the MAI or ALFA^2 thruster as closely as possible. The two components of the model are described in the following sections.

1. Channel Network

Figures 4 and 5 represent a section of the vaporizer tube and cathode tube which has been cut axially, along with its corresponding resistive network. The channel height, channel width, and groove width are given by a, b, and c respectively. The shaded regions represent cross sections of a helical channel through which lithium flows into (or out of) the page. Figure 6 shows a portion of the vaporizer tube with a single, helical vaporizer channel. At a given axial position (x coordinate), conservation of energy is applied through a volume with a perimeter indicated by the rectangular dotted line and a depth Δs along the channel (flow path) coordinate (s coordinate). The axial and channelwise coordinates, x and s, are as shown in Fig. 6. This figure also shows the outline of a representative control volume element. The channel and groove widths (b' and c') which define the control volume are slightly smaller than the values (b and c) measured in an axial cross section (Fig. 4) because of the angle introduced by the groove pitch p. The pitch shown in Fig. 6 corresponds to a single lead or channel. For cases with multiple channels, the pitch for that specific channel is used to correctly relate the fluid path length to cathode length along the x coordinate [i.e., $x = x(s, p)$]. The step length Δs (along the channel) is taken to be a small fraction of the channel width ($\Delta s \ll b$) so that a planar geometry for the control volume can be assumed.

The temperatures represented in the network and the corresponding heat flow vectors are also shown in Fig. 4. The direction of the heat flow vectors in the figure correspond to what has been taken as the positive sense. In generating the vaporizer performance curves, heat flux to the inner wall of the vaporizer tube is the independent variable and assumed uniform along the length of the vaporizer tube. Heat flows radially outward from the inner vaporizer tube wall, through the groove and fluid into the cathode tube. The equivalent resistive network for this system is shown in the schematic in Fig. 5. The node representing the outer wall temperature is connected to one of the two circuit elements as shown depending on whether the point of integration is under the flange.

The region of the flow under the mounting flange presents a unique challenge. The heat flow in this region is inherently multi-dimensional since elements of the network will see different thermal resistances to the radiating surfaces at each of the flange faces. To approximate this variation, an approach was adopted in which the flange is represented by four separate nodes (network B in Fig. 5).

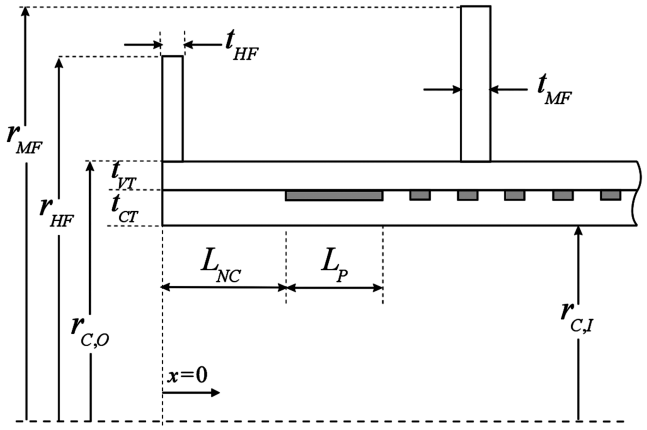

Fig. 3 Representative cross section of vaporizer tube showing prechannel region which includes the lithium pool, heater flange, and mounting flange.

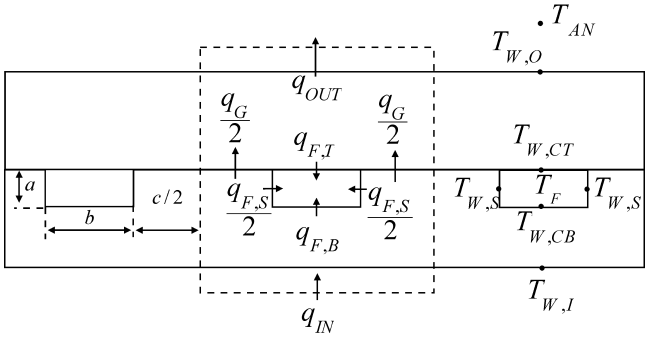

Fig. 4 Schematic of the vaporizer section in region with channels.

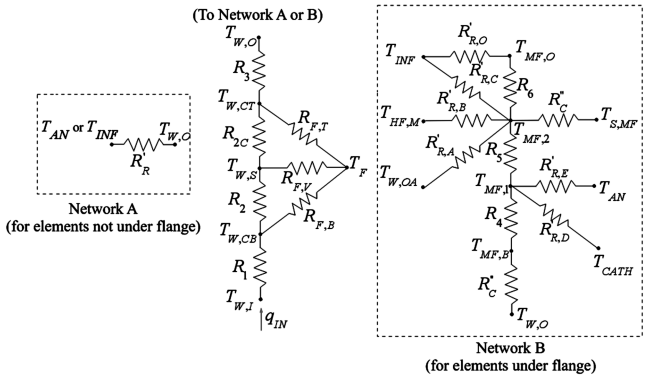

Fig. 5 Resistive network representation of vaporizer section in region with channels. The heat flow path out of the cathode tube changes depending on whether or not the element is under the flange.

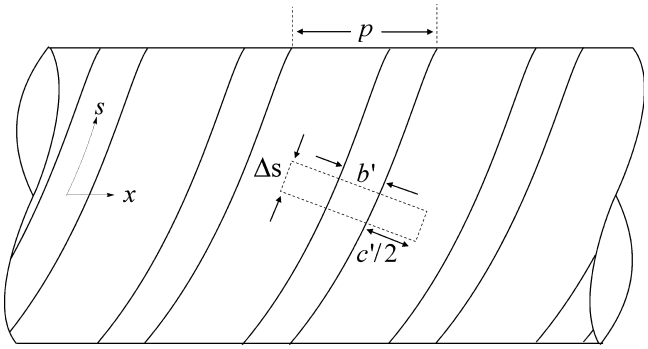

Fig. 6 Segment of vaporizer tube showing element of vaporizer channel used in thermal network analysis.

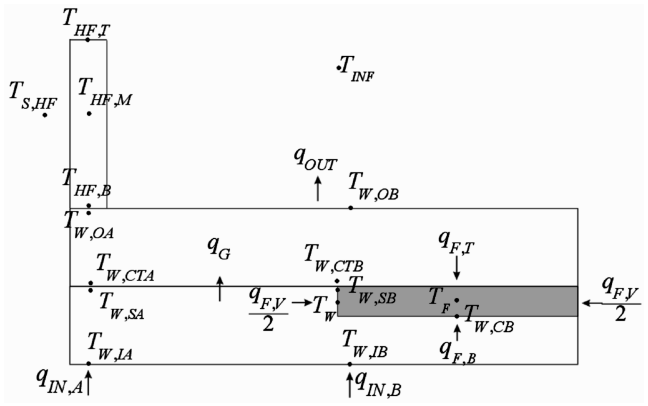

Fig. 7 Schematic of vaporizer section in prechannel region.

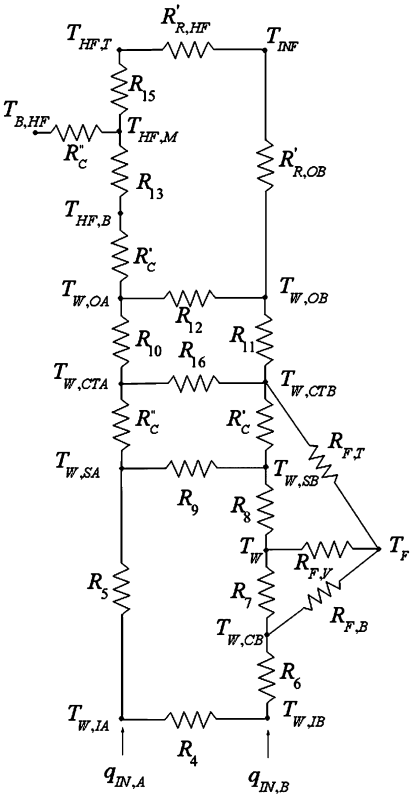

Fig. 8 Resistive network representation of vaporizer section in prechannel region.

These four nodes are located at the inner and outer radii (MF, *B* and MF, *O*), as well as at two equally spaced radial locations within the flange (MF, 1 and MF, 2). The radiation view factors from these surfaces to the surroundings, including the upstream cathode tube (view A), heater flange (view B), the vacuum chamber (view C), the downstream cathode tube (view E), and the anode (view E), were calculated from closed form analytical expressions for the approximate geometry as described in Sec. II.D. The three radiating surfaces of the mounting flange are the upstream and downstream facing surfaces (ΔA_{UP} and ΔA_{DN}, respectively) and the outer facing rim surface (ΔA_{RIM}). These surfaces are divided into a number of smaller area elements equal to the number of network elements under the flange. So for example, if each fluid channel has 270 elements or integration steps under the flange, and there are four channels, then the fraction of the area on each face used in the network system solution for one of the integration steps will be equal to $1/(4 \times 270) = 1/1080$th of the total surface area for that face. The surface of the mounting flange in contact with the mounting bus bar (ΔA_{COND}) is also handled in this manner.

This is only an approximate approach for a number of reasons. First, the view factors used correspond to those calculated for the entire face area, and second, this approach assumes each element under the flange will have the same thermal resistance to the radiating surface, regardless of whether it is right under an edge or under the middle of the flange. To the accuracy of the network model as a whole, the authors believe this approximation is reasonable. In particular, this approach allows both conduction and radiation heat loss from each fluid element under the flange to be captured. In addition, the approach captures the fact that different elements of the flange radiating surfaces will be at different temperatures as a result of the fluid below it.

The temperatures at the inner and outer wall of the vaporizer tube, the temperature of the cathode tube outer wall, and the heat flow into the fluid are determined by solving the system of equations for the network. This process is iterative because of the nonlinear temperature dependence of the radiative thermal resistance at the outer wall as will be discussed. After calculating the heat flow into the fluid, the increase in fluid temperature in a single phase region (or increase in the latent heat in the multiphase region) for the next element can be determined. This process is repeated, integrating along the channel length until the desired thermodynamic end state is reached.

At each station along the integration path, the fluid quality is determined and an appropriate convection heat transfer correlation applied. Once the end state is reached, the assumed heat flux (from the electric heater) is used to determine the required heater power for the calculated vaporizer length. The model results are typically presented as plots of vaporizer tube length vs heater power for different emissivities, mass flow rate, or other design parameters.

2. *Pre-Channel Network*

In the channel network just described, the network equations are solved at different locations along the channel to determine the axial temperature profile. In the prechannel region, there is no axial temperature profile calculated. Rather, the set of conservation equations is solved once in order to estimate the heat loss through this portion of the vaporizer tube, and also to calculate the temperature of the fluid at the point where it enters the vaporizer channels. The liquid pool acts as an inlet plenum. The low mass flux through this pool (due to a larger cross-sectional flow area) can result in significant heating of the fluid. The possibility of premature boiling in this pool region is something to be avoided as it will result in unsteady flow.

The prechannel portion of the vaporizer tube and its corresponding resistive network is shown in Figs. 7 and 8. The multidimensional geometry is captured in an approximate way in the thermal resistances used in the network equations. For example, the flange surface area (facing downstream) increases the surface area available for radiative emission, which lowers the impedance to radiation. In addition, the upstream facing flange area is clamped down to a base temperature $T_{S,\mathrm{HF}}$ through a contact resistance. Another feature of the prechannel region is the location of the pool, which is not centered in the control volume (only one bounding channel side is included in the schematic of Fig. 7). The pool actually is bounded by a channel wall on the downstream side (on the right in Fig. 7). This is accounted

for by using the area of both channel walls in the thermal resistance $R_{F,V}$. In Fig. 7, the feed tube geometry is not included. Any heat that bleeds out of the prechannel region through the feed tube will mostly serve to preheat the inlet fluid, and thus have little or no impact on the overall thermal efficiency of the vaporizer. In addition, the feed tube cross-sectional area is very small (less than 1% of the prechannel region). This simplification allows us to neglect the effect of the feed tube in the prechannel resistive network, thus preserving axial symmetry in calculating the thermal resistances.

In the prechannel region, axial heat flow paths are included in the network system. In Fig. 8, we see that the network is divided into two segments. Segment A is the portion of the cathode tube and vaporizer tube directly under the heater flange. Segment B includes all of the remaining cathode assembly in the prechannel region, including the inlet plenum. To better estimate the heat lost through the contact surface $T_{S,\mathrm{HF}}$, these two regions are coupled by including axial heat flow resistances.

The resistances used in the different sections are significantly different as seen in Tables 1 and 2. The entire prechannel portion of the vaporizer tube is solved with one resistive network. Therefore, a planar geometry cannot be assumed as is done in the channel network in which the conservation of energy is applied to what are essentially differential rectangular elements along the fluid path. The thermal resistances developed for the prechannel therefore reflect this radial geometry.

C. Convective Heat Transfer Coefficients

Correct evaluation of the heat transfer coefficients is critical if one is to gain useful insight into the performance characteristics of the vaporizer. Because they define the resistance of the heat flow into the fluid, the heat transfer coefficients will determine the locations of the boiling and dryout points, and will ultimately govern the overall length and thermal efficiency of the vaporizer.

1. *Liquid Region*

In the prechannel portion of the vaporizer, as well as in the region of the channels where the flow is entirely liquid (from fluid inlet to the onset of boiling), the correlation employed comes from Sleicher and Rouse [8], formulated specifically for low Prandtl number fluids ($Pr \ll 1$), and is given by

$$Nu = 6.3 + 0.167\, Re_D^{0.85} Pr^{0.93} \tag{1}$$

Here, Re_D is evaluated at the bulk temperature, and the Prandtl number is evaluated at the local wall surface temperature, which is taken to be a weighted average over all four channel walls at a given position along the channel. Additionally, to calculate the Reynolds number in the prechannel region, the area used for calculating the hydraulic diameter is the axial cross section of the liquid pool. Because the flow model is one-dimensional, the bulk temperature of the element is taken to be the local fluid temperature at that given position. The significant increase in fluid temperature from the feed tube inlet to the onset of boiling ($\sim$1100 K) makes capturing the effects of temperature-dependent fluid properties important.

2. *Multiphase Region*

In the multiphase region, two heat transfer mechanisms interplay to account for the total heat transfer into the fluid [9]. Initially, nucleate boiling will dominate the boiling regime. The second mechanism is convective boiling which is due to convection from the channel wall into a vapor film and then into entrained liquid droplets in the core of the flow. No and Kazimi's correlation accounts for these effects and was developed specifically for calculating the boiling heat transfer of liquid metals [10]. The correlation takes the form

$$Nu = 0.152 \frac{F_1}{F_2} Pr_L Re_{D_L}^{0.90} \phi_L \tag{2}$$

Table 1 Definition of the resistance in the prechannel network equations

Resistor	Equation	Resistor	Equation
R_4	$\frac{L_{\mathrm{NC}}-t_{\mathrm{HF}}}{\pi[(r_{C,I}+t_{\mathrm{VT}}-a)^2-r_{C,I}^2]k_{\mathrm{VT}}}$	R_5	$\frac{1}{2\pi t_{\mathrm{HF}}k_{\mathrm{VT}}}\ \ell_{\mathrm{n}}\left(\frac{r_{C,I}+t_{\mathrm{VT}}}{r_{C,I}}\right)$
R_6	$\frac{1}{2\pi(L_{\mathrm{NC}}+L_P-t_{\mathrm{HF}})k_{\mathrm{VT}}}\ \ell_{\mathrm{n}}\left(\frac{r_{C,I}+t_{\mathrm{VT}}-a}{r_{C,I}}\right)$	R_7	$\frac{1}{2\pi(L_{\mathrm{NC}}-t_{\mathrm{HF}})k_{\mathrm{VT}}}\ \ell_{\mathrm{n}}\left(\frac{r_{C,I}+t_{\mathrm{VT}}-0.5a}{r_{C,I}+t_{\mathrm{VT}}-a}\right)$
R_8	$\frac{1}{2\pi(L_{\mathrm{NC}}-t_{\mathrm{HF}})k_{\mathrm{VT}}}\ \ell_{\mathrm{n}}\left(\frac{r_{C,I}+t_{\mathrm{VT}}}{r_{C,I}+t_{\mathrm{VT}}-0.5a}\right)$	R_9	$\frac{(L_{\mathrm{NC}}-t_{\mathrm{HF}})}{\pi[(r_{C,I}+t_{\mathrm{VT}})^2-(r_{C,I}+t_{\mathrm{VT}}-a)^2]k_{\mathrm{VT}}}$
R_{10}	$\frac{1}{2\pi t_{\mathrm{HF}}k_{\mathrm{CT}}}\ \ell_{\mathrm{n}}\left(\frac{r_{C,O}}{r_{C,I}+t_{\mathrm{VT}}}\right)$	R_{11}	$\frac{1}{2\pi(L_{\mathrm{NC}}+L_P-t_{\mathrm{HF}})k_{\mathrm{CT}}}\ \ell_{\mathrm{n}}\left(\frac{r_{C,O}}{r_{C,I}+t_{\mathrm{VT}}}\right)$
R_{12}	$\frac{(L_{\mathrm{NC}}-t_{\mathrm{HF}})}{\pi/2[r_{C,O}^2-(r_{C,I}+t_{\mathrm{VT}})^2]k_{\mathrm{CT}}}$	R_{13}	$\frac{1}{2\pi t_{\mathrm{HF}}k_{\mathrm{HF}}}\ \ell_{\mathrm{n}}\left(\frac{r_{C_O}+0.5(r_{\mathrm{HF}}-r_{C,O})}{r_{C,O}}\right)$
R_{15}	$\frac{1}{2\pi t_{\mathrm{HF}}k_{\mathrm{HF}}}\ \ell_{\mathrm{n}}\left(\frac{r_{\mathrm{HF}}}{r_{C,O}+0.5(r_{\mathrm{HF}}-r_{C,O})}\right)$	R_{16}	$\frac{(L_{\mathrm{NC}}-t_{\mathrm{HF}})}{\pi/2[r_{C,O}^2-(r_{C,I}+t_{\mathrm{VT}})^2]k_{\mathrm{CT}}}$
$R'_{R,\mathrm{OB}}$	$\frac{T_{W,\mathrm{OB}}^{*3}}{\sigma\varepsilon 2\pi r_{C,O}(L_{\mathrm{NC}}+L_P-t_{\mathrm{HF}})}$	$R'_{R,\mathrm{HF}}$	$\frac{T_{\mathrm{HF},T}^{*3}}{\sigma\varepsilon 2\pi r_{\mathrm{HF}}t_{\mathrm{HF}}}$
$R_{F,T}$	$\frac{1}{2\pi h_F(r_{C,I}+t_{\mathrm{VT}})L_P}$	$R_{F,V}$	$\frac{1}{4\pi h_F(r_{C,I}+t_{\mathrm{VT}}-a/2)a}$
$R_{F,B}$	$\frac{1}{2\pi h_F(r_{C,I}+t_{\mathrm{VT}}-a)L_P}$		

Table 2 Definition of the resistance in the prechannel network equations

Resistor	Equation	Resistor	Equation
R_1	$\frac{t_{\mathrm{VT}}-a}{k_{\mathrm{VT}}(b'+c')\Delta s}$	R_2	$\frac{a}{2k_{\mathrm{VT}}c'\Delta s}$
R_{2C}	$\frac{1}{c'\Delta s}\left(\frac{a}{2k_{\mathrm{VT}}}+R''_C\right)$	R_3	$\frac{t_{\mathrm{CT}}}{k_{\mathrm{CT}}(b'+c')\Delta s}$
$R_{F,B}$	$\frac{1}{h_F b'\Delta s}$	$R_{F,T}$	$\frac{1}{h_F b'\Delta s}$
$R_{F,V}$	$\frac{1}{2h_F a\Delta s}$	R'_R	$\left[\frac{1}{\varepsilon_{\mathrm{CT}}}+\frac{r_{C,O}}{r_{\mathrm{AN}}}\left(\frac{1}{\varepsilon_{\mathrm{AN}}}-1\right)\right]T_{W,O}^{*3}/\sigma\Delta s(b'+c')$
R_4	$\frac{r_{\mathrm{MF}}-r_{C,O}}{3k_{\mathrm{MF}}(b'+c')\Delta s}$	R_5	$\frac{r_{\mathrm{MF}}-r_{C,O}}{3k_{\mathrm{MF}}(b'+c')\Delta s}$
R_6	$\frac{r_{\mathrm{MF}}-r_{C,O}}{3k_{\mathrm{MF}}(b'+c')\Delta s}$	$R_{R,O}$	$\frac{T_{\mathrm{MF},O}^{*3}}{\sigma\varepsilon F_T\Delta A_{\mathrm{RIM}}}$
$R'_{R,A}$	$\frac{T_{\mathrm{MF},2}^{*3}}{\sigma\varepsilon F_A\Delta A_{\mathrm{UP}}}$	$R'_{R,B}$	$\frac{T_{\mathrm{MF},2}^{*3}}{\sigma\varepsilon F_B\Delta A_{\mathrm{UP}}}$
$R'_{R,C}$	$\frac{T_{\mathrm{MF},2}^{*3}}{\sigma\varepsilon F_C\Delta A_{\mathrm{UP}}}$	$R'_{R,D}$	$\frac{T_{\mathrm{MF},1}^{*3}}{\sigma\varepsilon F_D\Delta A_{\mathrm{DN}}}$
$R'_{R,E}$	$\frac{T_{\mathrm{MF},1}^{*3}}{\sigma\varepsilon F_E\Delta A_{\mathrm{DN}}}$	$R_{C,\mathrm{BB}}$	$R''_C/\Delta A_{\mathrm{COND}}$

where, the subscript "L" refers to the conditions of the saturated liquid. The Reynolds number is based on the liquid mass flux,

$$Re_{D_L} = \frac{G(1-X)D_h}{\mu_L} \tag{3}$$

where the liquid mass flux is weighted by the vapor quality. The mass flux used to calculate the Peclet number below is also corrected in this manner.

In the correlation given by Eq. (2), the parameter ϕ_L represents an empirical correction factor developed by Zeigarnick and Litvinov [10] [Eq. (5)] in terms of the Martinelli parameter [Eq. (6)]. This parameter is defined as

$$\phi_L = (\phi_L)_{tt}^{0.88} \tag{4}$$

where

$$(\phi_L)_{tt} = \left[1 + \frac{20}{X_{tt}} + (X_{tt})^{-2}\right]^{1/2} \tag{5}$$

$$X_{tt} = \left(\frac{1-X}{X}\right)^{0.9}\left(\frac{\rho_V}{\rho_L}\right)^{0.5}\left(\frac{\mu_L}{\mu_V}\right)^{0.1} \tag{6}$$

The values for F_1 and F_2 are dependent on Re_{D_L} and are obtained from the following expressions:
For $Re_{D_L} < 50$

$$F_1 = 1.5, \qquad F_2 = 0.7071(Re_{D_L})^{0.5} Pr_L \tag{7}$$

For $50 \le Re_{D_L} \le 1125$

$$F_1 = 1.563, \qquad F_2 = 5Pr_L + \left(\frac{5}{E}\right)\ell_n\left[1 + E\,Pr_L\left(\frac{\delta_C^+}{5} - 1\right)\right] \tag{8}$$

For $Re_L > 1125$

$$\begin{aligned} F_1 &= 1.818 \\ F_2 &= 5Pr_L + \left(\frac{5}{E}\right)(1 + 5E\,Pr_L) \\ &\quad + \left(\frac{6}{E\gamma}\right)\ell_n\left[\left(\frac{2M+\gamma-1}{1+\gamma-2M}\right)\left(\frac{1+\gamma-\beta}{\beta+\gamma-1}\right)\right] \end{aligned} \tag{9}$$

The additional parameters used in these relations are defined as follows:

$$E = 0.00375\ Pe_{D_L}[1 - \exp(-0.00375 Pe_{D_L})] \tag{10}$$

$$\delta_C^+ = 0.4818(Re_{DL})^{0.585} \tag{11}$$

$$\gamma = \left[1 + \left(\frac{10M}{E\delta_N^+ Pr_L}\right)\right]^{0.5} \tag{12}$$

$$M = 1 - (\alpha)^{0.5} \tag{13}$$

$$\alpha = \left[1 + \left(\frac{1-X}{X}\right)\left(\frac{\rho_V}{\rho_L}\right)\right]^{-1} \tag{14}$$

$$\delta_N^+ = 0.133(Re_{D_L})^{0.7614} \tag{15}$$

$$\beta = 60\left(\frac{M}{\delta_N^+}\right) \tag{16}$$

From Eqs. (2–6), we see that the Nusselt number calculated using this correlation has a strong dependence on the vapor mass fraction. As the vapor fraction approaches one (full vaporization), both the liquid phase Reynolds number and the Martinelli parameter approach zero. Although somewhat offset by the Reynolds number approaching zero, the Martinelli parameter in the denominator of the Zeigarnick and Litvinov factor of Eq. (5), can cause this correlation to predict unreasonably high heat transfer coefficients for high values of the vapor fraction ($X > 0.96$).

3. *Vapor Region*

In the vapor region, the flow remains laminar and has a Prandtl number of order 1. The Nusselt number for this fully developed flow will tend to be a constant value determined only by the channel's cross-sectional aspect ratio (a/b' from Figs. 4 and 6). The Nusselt number used for the simulation was obtained by interpolation of the channel geometries listed in Holman [11]. For the baseline channel geometry of the ALFA^2 vaporizer, the value of the heat transfer coefficient is calculated from $Nu = 4.95$.

D. Solution Methodology and Boundary Conditions

1. *Pre-Channel Region*

The prechannel region, which includes the heater flange, liquid inlet, and the liquid annulus, is divided into two segments; a portion which includes the inlet plenum, and a slice under the heater flange (Fig. 7). The fraction of the total heater power into these two segments ($q_{\mathrm{IN},A}$ and $q_{\mathrm{IN},B}$) and the fluid inlet temperature (T_{IN}) are used as the independent variables in the network equation. The heat into this region is calculated from a given heater flux, and the inlet temperature is taken to be only slightly greater than the melting point of lithium ($T_{\mathrm{IN}} = 500$ K). On the outer cathode surface, a radiation boundary condition to the vacuum chamber is applied with view to a 300 K ambient condition. The prechannel cathode area emits to a blackbody enclosure, assuming the surface area of the vacuum chamber is much larger than the cathode surface area. To the left of the heater flange, a heat sink of 1000 K is included to account for heat loss through conduction to a mounting surface.

To obtain the solution for the prechannel portion of the vaporizer, the system of equations based on the resistive network from Fig. 8 is solved using Matlab. The radiation resistances, $R'_{R,\mathrm{OB}}$ and $R'_{R,\mathrm{HF}}$ are introduced in the network equation to linearize the nonlinear temperature dependence of the radiation boundary conditions. By grouping terms which include the wall temperature into the radiation resistances as shown in Table 1, the equation network is linearized with the penalty of making the coefficient matrix a function of the unknown surface temperature. This requires that the network equation be solved iteratively. By providing an initial estimate for the outer wall temperatures $T^*_{W,\mathrm{OB}}$ and $T^*_{\mathrm{HF},T}$, an estimated value for the linear radiation resistance can be calculated in the coefficient matrix. After solving the system of equations based on this "guess," the calculated wall temperatures are compared with the initial guess to test convergence. If this comparison satisfies the convergence criterion, the solution for the prechannel is stored and becomes the inlet condition for the channel region. If it does not, the calculated values for $T_{W,\mathrm{OB}}$ and $T_{\mathrm{HF},T}$ become the updated "guesses" for the next iteration, the resistances are recalculated, and the process is repeated until the convergence criterion is satisfied. Because there is a relatively small temperature gradient throughout the entire cathode cross section, the convergence criterion is chosen to be very small. For all simulations, the convergence criterion was set to 1×10^{-9} K.

2. *Channel Region*

The solution for the resistive network in the channel region is obtained in a different manner from the prechannel region. In the channel region, the network equation is still solved iteratively, as described above, but for each differential element (shown in Fig. 6) along the path coordinate s. Consistent with the planar geometry assumption, extremely small integration steps were employed ($\Delta s \approx 0.1$ mm) in the simulations. An additional unknown q_H is included in the network equation in order to explicitly calculate the magnitude of the heat passing into the fluid. At each element in the channel, the fluid temperature for the next step is updated based on a

calculated temperature gradient ΔT_F. This updated value for the fluid temperature is then used to calculate the relevant set of material properties based on relations from Jeppson [12] and Yih [13], and used as the independent variable (along with q_{IN}) in the next solution step. Tungsten properties used in the simulation are also temperature dependent. An average temperature throughout each component (i.e., cathode tube, vaporizer tube, and flanges) is used to calculate its thermal conductivity, and the outer surface temperature is used to calculate a temperature-dependent surface emissivity. Also, while the mass flow rate through the prechannel section is the total overall mass flow rate through the vaporizer (for the baseline ALFA^2 design, $\dot{m} = 80$ mg/s), the portion of this mass flow through each of the individual channels is the total divided by the number of channels. This makes use of the assumption that the mass flux is divided uniformly over each of the channels.

As the solution point moves axially through the channel region, the radiation view from the outer surface of the cathode switches from the laboratory environment to the anode assembly (shown conceptually in Fig. 1). To the left of (and including) the mounting flange, the radiation heat transfer is treated as emission to a large surrounding enclosure at 300 K (which is treated as a blackbody). To the right of the mounting flange, the cathode assembly is surrounded by either an insulator (ALFA^2 design) or a tungsten grounding screen (MAI design). In this region, the radiation view changes to 600 K and is modeled as two emitting, infinite, concentric cylinders (i.e., the view factor from cathode to anode is assumed equal to unity). This simplification is valid for the reasonably large aspect ratio of the cathode assembly ($L/r_{C,O} \approx 10$) and the relative proximity of the anode to the cathode.

The mounting flange is also located in the channel region. In the segment under this flange, the network equation changes due to the conduction heat path to the bus bar, as well as the additional equations governing the multiple radiation views. As seen in Fig. 9, over its entire upstream facing surface area, the mounting flange has view to the outer cathode tube, heater flange, as well as the vacuum chamber. The temperatures of these surfaces are known, either from the solution to the prechannel region (cathode tube $T_{W,\text{OB}}$ and heater flange $T_{\text{HF},M}$) or from simulation inputs (chamber temperature T_{INF}). On the downstream facing side, the mounting flange surface has different boundary conditions on its upper and lower halves. On the lower half, the flange has view to an insulator or grounding screen and the hot end of the cathode tube. The insulator temperature is also a simulation input, but the temperature for the downstream end of the cathode tube T_{CATH} must be supplied a priori. Because the multiphase fluid regime ($T_F = 1620$ K) dominates the portion of the vaporizer downstream of the mounting flange, a reasonable value for this radiation view is assumed to be 1600 K. Subsequent checks of this assumption validate the usage of this temperature. The remaining upper half of the mounting flange (facing downstream) is in direct contact with an actively cooled cathode mounting plate (bus bar). Over this surface, a 500 K conduction boundary condition is used to simulate parasitic heat losses to the cathode mounting plate (bus bar). Because this plate/flange interface will need to conduct several thousand amperes of current from the bus bar to the cathode, it is not practical to increase the thermal resistance to this flange by using an insulating plate. The outer radius/rim of the flange is assumed to emit only to the environment/chamber. To calculate the various view factors, closed form expressions for the representative flange areas are taken from Naraghi and Chung [14] for a class of annular disks emitting to axisymmetric bodies (i.e., cylinders and cones), from which, the individual view factors to each of the components are calculated.

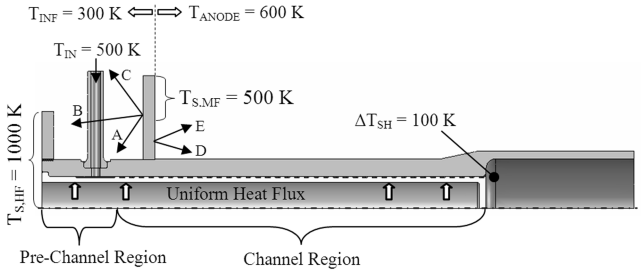

Fig. 9 Cathode assembly showing boundary conditions and thermodynamic end state for the baseline case.

When the fluid temperature reaches the saturation temperature ($T_{\text{SAT}} = 1620$ K at 1 atm), the simulation moves into the multiphase region, and new correlations are employed. In this multiphase region, the network equation solved is modified slightly to account for the fact that heat into the fluid results in an increase in latent heat rather than an increase in the temperature. To account for this, the coefficient matrix is altered to reflect the constraint $\Delta T_F = 0$. Within this phase change region, the value of the vapor mass fraction is calculated at each step by the evaluating the ratio of the latent heat absorbed by the two-phase mixture to the total amount of latent heat required to complete the phase change (i.e., to achieve dryout). This ratio is the vapor mass fraction or quality used earlier:

$$X = \frac{lh_{\text{absorbed}}}{\dot{m} \cdot h_{fg}} \tag{17}$$

where h_{fg} is the latent heat of vaporization [J/kg], and lh_{absorbed} is an integration of q_H [W] over the fluid path. The value for the vapor mass fraction (or quality) is used to determine the completion of the phase change (dryout point) and monitor any potential recondensation under the flange. When $X = 1$, the boiling process is complete, and the simulation begins using the vapor phase correlations.

The simulation parameters and the assumed values for the MAI and ALFA^2 vaporizers are shown in Tables 3 and 4. These values were selected to best represent the actual parameters for the MAI [14] and ALFA^2 thruster. For the MAI vaporizer, the vaporizer tube is made from molybdenum and the cathode tube is constructed from tungsten. The conceptual ALFA^2 design is an all tungsten construction. Properties for tungsten, including emissivity and thermal conductivity, are temperature dependent and taken from Yih and Wang [13]. For the temperatures throughout the cathode assembly, the range of surface emissivity and thermal conductivity are 0.08–0.24 and 103–137 W/mK, respectively. The value for the thermal contact resistance was estimated based on an order of magnitude comparison with similar metal-to-metal contact surfaces from Holman [11]. A baseline exit condition for vapor superheat was taken to be 100 K for all cases. The component arrangement and dimensions for the analysis were selected so as to approximate the preliminary design to be used in initial testing, not the conceptual design shown in Fig. 1. Any of these parameters can be changed to quickly test the effect on the vaporizer performance.

III. Results from Network Model

A vaporizer performance curve represents the locus of length-power solutions for a range of heat flux values. The knee in these curves represents the optimal solution from a thermal efficiency standpoint. Above the knee, the upper right portion of the curve represents the low-flux, long-length solution branch. Below the knee, the lower right portion of the curve represents the high-flux, short-length solution branch. Either of these branches represents a departure from optimal thermal efficiency, either because the higher outer wall temperatures (lower branch) or large surface area (upper branch) increases the radiation losses. There are a number of unknown parameters from the MAI tests which are inputs to the model and could affect this comparison. Among others, these include the vapor superheat for each case and the boundary conditions on the flanges. In these instances, assumed values were used and taken to be equivalent to the ALFA^2 baseline case (shown in Fig. 9).

Figure 10 shows the results of this model compared with experimental data for 5 tests of the MAI 200 kW thruster (Table 5). The eight flow rates represent the minimum–maximum bounds for the five tests shown in Table 5. All five tests were conducted using the same power and length, so the eight flow rates shown in Table 5 correspond to a single data point in Fig. 10. While showing an overall

Table 3 MAI parameter list[a]

Geometry	Value	Conditions/Properties	Value/Range
a	2.0 mm	$\varepsilon_{CT} = \varepsilon_t(T)$	0.08–0.24
b	4.0 mm	ε_{AN}	0.7
c	2.0 mm	R''_C	7.0×10^{-6} m^{-2}-K/W
t_{VT}	4.0 mm	T_{IN}	500 K
t_{CT}	3.5 mm	T_{AN}	600 K
$r_{C,I}$	15 mm	ΔT_{SH}	100 K
r_{AN}	48 mm	k_m	98 W/m-K
L_{NC}	18 mm	$k_t = k_t(T)$	103–137 W/m K
L_P	30 mm	Channels	3

[a]For 3 channels, $p = 18$ mm, $b' = 3.95$ mm, $c' = 1.975$ mm.

Table 4 Baseline ALFA^2 parameter list[a]

Geometry	Value	Conditions/Properties	Value/Range
a	0.75 mm	$\varepsilon_{CT} = \varepsilon_t(T)$	0.08–0.24
b	2.5 mm	ε_{AN}	0.7
c	2.5 mm	R''_C	7.0×10^{-6} m^{-2}-K/W
t_{VT}	3.0 mm	T_{IN}	500 K
t_{CT}	9.0 mm	T_{AN}	600 K
$r_{C,I}$	13.5 mm	ΔT_{SH}	100 K
r_{AN}	58 mm	k_m	98 W/m-K
L_{NC}	14.2 mm	$k_t = k_t(T)$	103–137 W/m K
L_P	20.2 mm	Channels	4

[a]For 4 channels, $p = 20$ mm, $b' = c' = 2.453$ mm.

Table 5 MAI Flow rate range and heater power during preheat phase [7][a]

Test	Minimum flow (mg/s)	Maximum flow (mg/s)	Heater power (W)
1	55	107	3600
2	96	106	3600
2	92	104	3600
3	104	125	3600
5	128	128	3600

[a]MAI vaporizer tube length = 21.0 cm.

agreement, the model underpredicts the power requirement for low mass flow rates and overpredicts the high flow rates. A likely cause for this trend is the constant thermodynamic end state that was used for all cases (i.e., 100 K superheated vapor). In reality, higher flow rates will have lower vapor superheat for a constant length and power. The effect of choosing too high of an end condition would be to bias the curves to the right, while choosing too low of an end condition would bias the curves to the left. Ideally, if the values for the superheated vapor for each flow rate that was tested were known, it would be expected that all the curves would approach a single power-length vaporizer curve.

The next six figures present the results of the network model for the conceptual ALFA^2 design. In Fig. 11, the sensitivity of vaporizer thermal performance to cathode tube emissivity is shown for the nominal flow rate of $\dot{m} = 80$ mg/s. For each individual curve, the value for emissivity is held constant (not temperature dependent). We can see in Fig. 11 that the emissivity of the outer cathode tube is a strong driver of the vaporizer thermal performance. The steepening of the curves, as well as the lower, optimal power point as the emissivity is decreased is a result of the increasing efficiency as more of the heat is captured by the fluid. The steepening of the curves as the emissivity is lowered shows that the vaporizer can operate more efficiently over a wider range of lengths. Also, one can see from Fig. 11 that lowering the emissivity tends to increase the optimal length. This is due to the fact that as the radiation heat loss is reduced, the longer length results in lower heat fluxes. This then results in lower prechannel temperatures, reducing the conduction heat loss out through the base of the heater flange. For the current ALFA^2 design, the vaporizer tube length is 22.86 cm which corresponds to a calculated heater power of approximately 3.9 kW (for a constant emissivity of 0.3).

A temperature-dependent emissivity for the outer cathode tube was used to obtain the curves in Figs. 12–16 (the range is reported in Table 4). Figure 12 shows the thermal performance sensitivity of the vaporizer to mass flow rate. For given initial and final thermodynamic states, the minimum power (vaporizer thermal efficiency 100%) scales linearly with the mass flow rate. This is evident in Fig. 12 from the nearly equal spacing of the curves. As a point of reference, at $\dot{m} = 80$ mg/s, the minimum power to vaporize the lithium is $P_{min} = 1.992$ kW, so the maximum vaporizer efficiency for assumed geometry and inlet/outlet states is approximately 60%. The slight variation in the shape of the curves is a result of second-order effects such as the change in convective heat transfer coefficient as the Reynolds number in the channels increase. This improvement in heat transfer results in the slight increase in the optimal length as the mass flow rate increases. Because less heat is radiated away in the regions of lithium flow (because more heat is absorbed into the fluid), a longer vaporizer tube lowers the required heater flux, which in turn lowers the surface temperature of the dead region in the prechannel region (i.e., the section which has no fluid flow, L_{NC} in Fig. 3). This aids in reducing

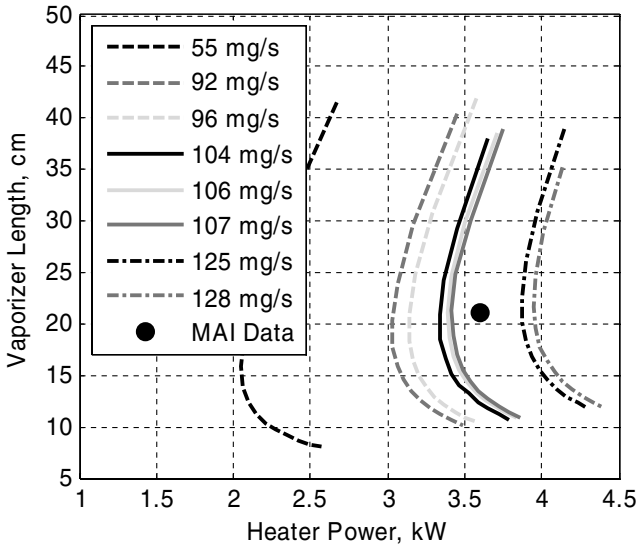

Fig. 10 Comparison of network model results with data from the 200 kW MAI thruster. The eight mass flow rates used to generate the vaporizer performance curves represent the range of flow rates in Table 5.

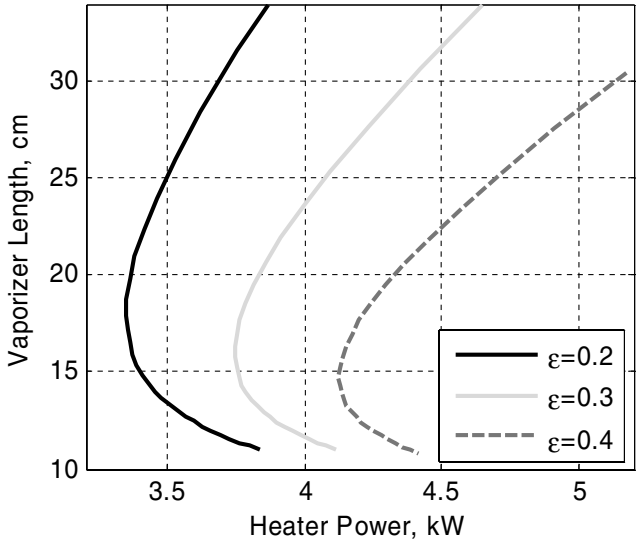

Fig. 11 ALFA^2 vaporizer power calculated using network model. Sensitivity to emissivity of cathode tube surface for nominal mass flow rate of $\dot{m} = 80$ mg/s.

the heat loss through radiation and through the conduction heat sink at the base of the flange.

In Fig. 13, we show the temperatures calculated with the channel network model as a function of axial position for the ALFA^2 baseline case listed in Table 4. The position coordinate begins at 3.44 cm which is the axial position corresponding to the transition between the prechannel and channel regions of the vaporizer. The inlet temperature to the channel is the calculated fluid temperature from the pool section. In Figs. 13 and 14, we have calculated the temperature profile out to approximately $x = 33$ cm (vapor superheat of 330 K) to capture the leveling off of the fluid temperature in the vapor region. For the ALFA^2 baseline parameters, the lithium is seen to be fully vaporized at a point 0.98 cm from the end of the vaporizer tube which has a length of $x = 22.86$ cm. In terms of the path length s along the channel, the dryout point is 4.9 cm from the channel exit to the end of the vaporizer tube. The discontinuities in the wall temperatures as the fluid moves under the flange and into the superheated region and is a direct result of neglecting any axial heat transfer in the channel region.

Figure 13 shows the temperature profile at the onset of boiling and through the region under the main mounting flange. Clearly visible in this plot is the effect of the 500 K heat sunk flange on the behavior of the temperature profile. In this region under the flange, the overall effect is to extract heat out of the fluid, initially causing fluid condensation (quality reduction). After all of the vapor has been converted back to liquid, the 500 K heat sink results in significant reductions in temperature of all components, as well as the fluid. In addition, the simulation shows only limited sensitivity to this boundary condition. If the temperature of this heat sink is doubled (1000 K), there is only a modest decrease in the power requirement of 3.9%. This result suggests that the conduction heat flow path through the mounting flange is a major driver of vaporizer performance.

The leveling of the temperature profile is a consequence of the decrease in the heat flux to the vapor as seen in Fig. 14. The discontinuities evident at the points where vaporization begins ($\sim$7.5 cm) and ends ($\sim$22 cm) are numerical artifacts that result from transitioning to different convection correlations at these points. Under the flange, however, the spikes in the heat flux are consistent with the modeling approach. In this region, the temperature of the cathode drops rapidly due to the 500 K contact surface of the flange. The fluid temperature, however, remains constant until the two-phase flow has fully condensed (i.e., reached a quality of zero). The large temperature gradients that result between the saturated fluid and the relatively cold walls are the cause for the large spikes in the heat flux (at $x \sim 5$ cm), and are a direct result of neglecting axial heat flow.

From this plot we also see that the largest source of thermal inefficiency is radiation losses from the cathode outer tube, a fact that was suggested by the sensitivity of the performance curves for different emissivities as previously discussed in reference to Fig. 11. In the superheated vapor region ($L > 22$ cm) we see that the heat flux into the vapor from the channel top and bottom ($q''_{\mathrm{FH},T}$ and $q''_{\mathrm{FH},B}$) and sides (q''_{FV}) approach zero. This is a consequence of the temperature difference between the channel walls and vapor approaching zero. Recall that the heat flux into the control volume is a constant. The heat flow into the fluid cannot increase without limit and some heat is always radiated away from the outer surface of the cathode tube. As the length increases, the fluid temperature will approach equilibrium with the channel walls and the outer surface temperature will steadily increase and approach a value such that all the additional supplied power is radiated away.

This behavior is further evident in Fig. 15 which presents the cost of the "safety margin" in terms of a percentage length increase and thermal efficiency as a function of vapor superheat. The percentage length increase is measured relative to the length needed to reach the dryout point, L_{DRY}, and is defined as $(L_{\mathrm{TOT}} - L_{\mathrm{DRY}})/L_{\mathrm{DRY}}$. From Fig. 13 for the baseline case, $L_{\mathrm{DRY}} = 21.88$ cm (along the x coordinate). Any increase beyond this point will add safety margin (with respect to liquid expulsion which should be avoided) but will also increase the surface area available for heat loss and will lower the thermal efficiency as shown in Fig. 15. Beyond 200 K of vapor superheat, the loss of efficiency becomes significant.

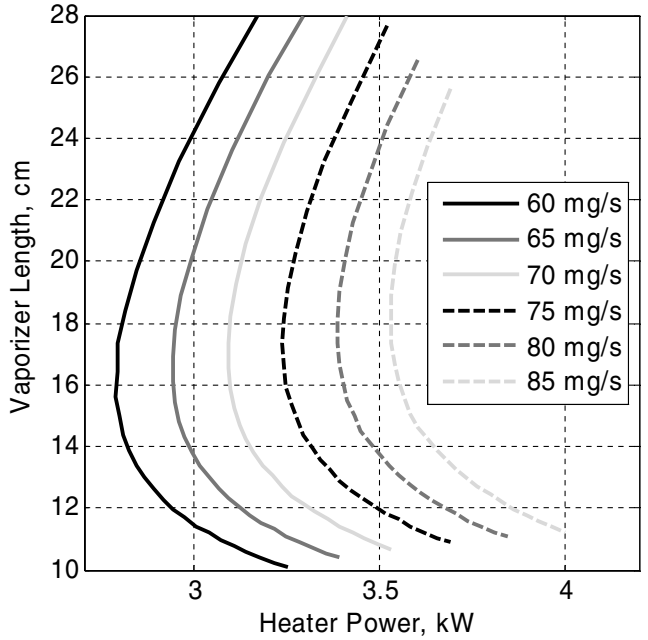

Fig. 12 ALFA^2 vaporizer power calculated using network model. Sensitivity to mass flow rate for a temperature-dependent emissivity.

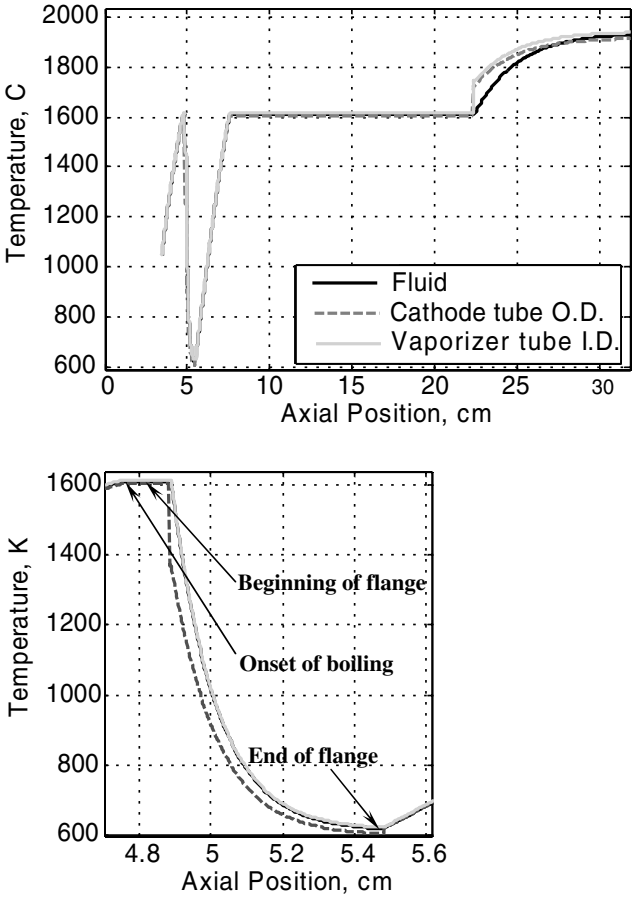

Fig. 13 Top: Calculated vaporizer tube, fluid, and cathode tube temperatures as a function of axial position for the case of vapor superheat of 330 K (baseline ALFA^2 length is 22.86 cm). Bottom: Expanded view of the region of condensation and temperature decrease of the lithium flow under the mounting flange.

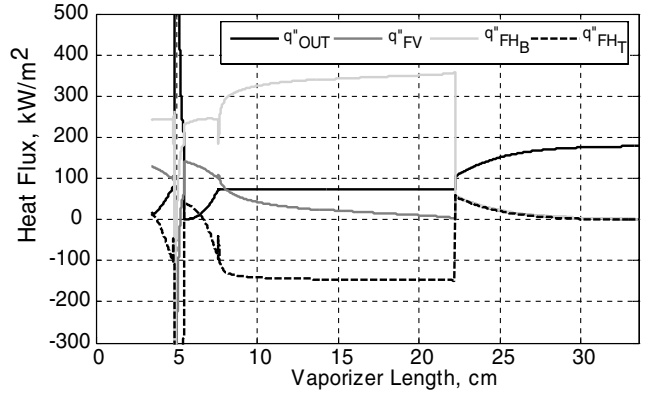

Fig. 14 Heat flow through the network as a function of axial position. To highlight the system's trends, the results are shown for a vapor superheat of 330 K. The baseline ALFA[2] parameters are listed in Table 4.

Finally in Fig. 16 we present the vaporizer length-power curves similar to those presented for the emissivity and mass flow rate sensitivity analysis. This curve provides an estimate of the increase in heater power needed to increase the level of vapor superheat for a given length. An estimate of what constitutes an acceptable safety margin will require some analysis of the flow instabilities which could lead to oscillation of the dryout point. If this fluctuation is large enough, liquid could be ejected into the plenum. If this information is available, the required margin can be expressed in terms of superheat and Fig. 16 consulted to estimate the heater power needed to provide that margin.

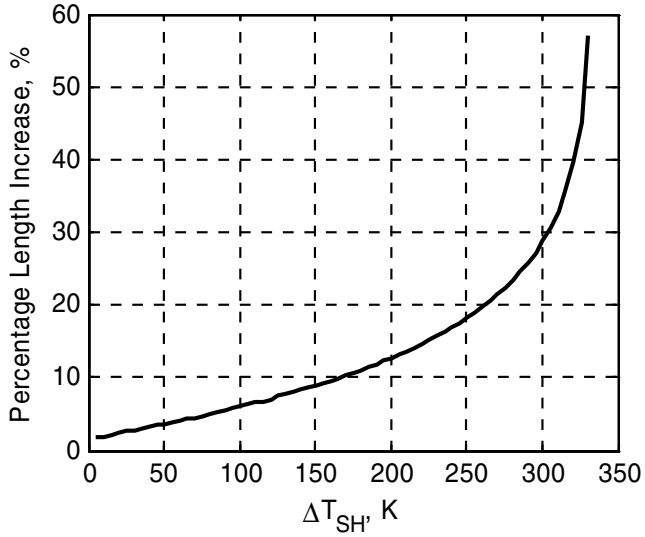

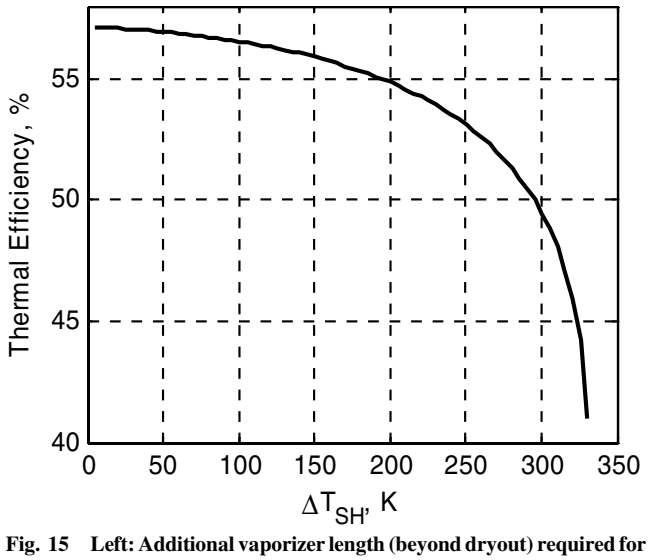

Fig. 15 Left: Additional vaporizer length (beyond dryout) required for various levels of vapor superheat. Right: Thermal efficiency as a function of vapor superheat. The plots asymptote due to a thermal equilibrium condition at a vapor superheat of approximately 330 K.

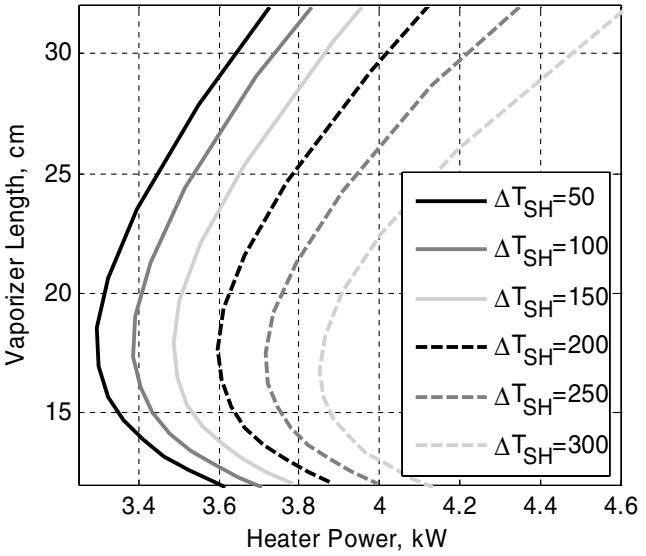

Fig. 16 ALFA[2] vaporizer power calculated using network model. Sensitivity to level of vapor superheat on the power/length requirements of vaporizer for nominal mass flow rate of $\dot{m} = 80$ mg/s.

IV. Finite-Element Thermal Model

The objective of this portion of the investigation was to create a finite-element thermal model (FETM) of the cathode subsystem. The FETM uses results of the network model calculation to provide a surface temperature distribution with a much higher level of spatial resolution. The results of this model can be used to update and refine the boundary conditions used for the network model.

The numerical FETM was developed using the SDRC IDEAS Thermal Modeling Group (TMG) commercial software package [15,16] to evaluate the vaporizer subcomponents. The FETM developed herein includes conduction and radiation heat transfer from, between, and within all of the major components of the cathode assembly. Modeling the helical channels in the vaporizer tube is a very challenging computational problem due to the extreme aspect ratio of the fluid channels ($L/D \sim 1000$). This aspect ratio (coupled with the inherent three-dimensionality of the vaporizer and flow channels) proves to be prohibitively expensive when attempting to mesh. Therefore, to include the effects of the two-phase fluid flow in the simulation, results from the network model were mapped to the IDEAS-TMG FETM. Figure 17 shows the methodology used to couple the results of the network model to the FETM through the channel portion of the vaporizer. Using a lumped parameter

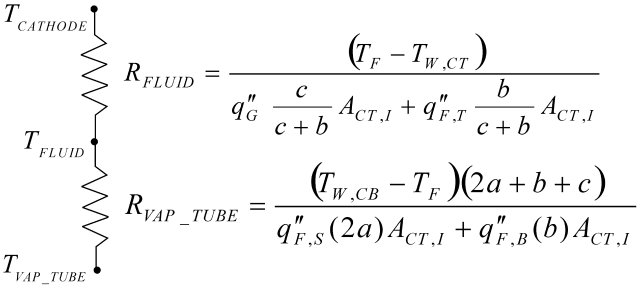

Fig. 17 TMG thermal couplings used to incorporate the network model fluid flow information.

approach, the heat flux to the inner vaporizer tube wall is applied as a boundary condition. Furthermore, the convective film coefficient along the vaporizer tube outer wall and the cathode tube inner wall are each prescribed per the network model. To eliminate the computational expense of meshing the fluid channels, these surfaces are modeled as concentric cylinders separated by the channel height.

To calculate the thermal resistance (coupling) between the fluid and cathode tube, R_{FLUID}, a weighted average of the heat flux through the solid grooves (q''_G) and the fluid (q''_{FT}) is used, as shown in Fig. 17, to capture the effects of the fluid channels on the heat flow. In this expression, it is seen that the heat fluxes into the fluid is subtracted from the heat flux out of the solid channel groove. This is due to the sign convention adopted for positive heat flow directions as shown in Fig. 4. To calculate the thermal resistance into the vaporizer tube $R_{\mathrm{VAP\_TUBE}}$ a weighted average of the heat flux through the channel sides (q''_{FS}) and bottom (q''_{FB}) is used. The fluid temperature calculated by the network model provides an additional constraint. At predetermined axial stations, TMG thermal couplings (conductances) are defined using the local fluid temperature and film coefficients predicted by the network model [note the film coefficients h are related to the thermal resistances by $h = 1/(RA)$]. A total of 29 such thermal couplings were employed in the axial direction in order to accurately resolve thermal gradients within the vaporizer tube/cathode annulus.

The fluid temperature profile obtained from the network model which was used as an input to the TMG model varied from a minimum of 1042 K in the reservoir region to a maximum of 1720 K at the downstream end of the vaporizer tube. Film coefficients obtained from the network model used as inputs into the FETM ranged from 66.5 $\mathrm{W/m^2}$-K to 2.27×10^8 $\mathrm{W/m^2}$-K along the axial length of the vaporizer tube/cathode tube annulus. The external boundary conditions have already been summarized in Fig. 9. Additional boundary conditions were applied to the left (upstream) side of the heater flange. The flange is conductively coupled to a 1000 K sink which represents an insulator plate which supports the heater element. The conductance out of the heater flange (to the 1000 K sink) was adjusted to match a heat flux of $43,959$ $\mathrm{W/m^2}$. This flux represents a loss of heat from the vaporizer to the structure which supports the heater. Also, the inner diameter of the vaporizer tube was exposed to a uniform heat flux of $179,100$ $\mathrm{W/m^2}$ which represents the radiation heat transfer to the inner vaporizer tube wall from the graphite heater. These values were calculated using the network model for the baseline ALFA^2 geometry.

In summary, the results from the network model are used to provide 1) the fluid temperature profile, 2) the values of conductance (or thermal resistance) as shown in Fig. 17, and 3) the heat flux out of the heater flange to the supporting structure. The FETM uses these inputs, along with view factors of a higher fidelity than the network model, to provide a solution of the temperature distribution over the complex structure which has a spatial resolution much finer than can be obtained with the network model alone. The converged grid independent model used in the FETM consisted of 234,179 finite elements. These results are presented in Sec. VI.

V. Methodology

A. Governing Equations

IDEAS-TMG uses an element-based finite-difference discretization technique to simulate conduction within the solid, as well as to model the radiation and convection from the solid model surfaces. The thermal solver employed by TMG uses a finite control volume (finite-difference) method to obtain the solution to the thermal model. The unstructured finite element mesh of the IDEAS meshing tool suite is used to discretize the thermal model. Solid conduction, surface convection, and surface radiation are simulated using this so-called "element-based finite-difference method". The TMG software employs a control volume approach to formulate the discrete finite-difference equations which approximate the governing partial differential equations. This method is also known as the lumped parameter method, and it encompasses the meshing of the model into control volume regions and establishing (in each region) a computation point called the finite-difference (FD) calculation point. The FD point is essentially a node with a thermal capacitance $C = mc$(m = mass, c = element's specific heat) equal to that of the control volume surrounding it. Heat balance equations are then built for each of these control volumes.

The generic heat balance equation for a given control volume is written as

$$\int_A q_n dA + \int_V q_o dV = \int_V \rho c \frac{dT}{dt} dV \tag{18}$$

which can also be expressed as

$$Q_b + Q_o = \frac{dU}{dt} \tag{19}$$

where Q_b is the heat flow across the control volume boundaries, Q_o is the heat generated within the control volume, and U is the energy stored within the control volume. Assuming a constant density within the control volume, Eq. (19) becomes,

$$\frac{dU}{dt} = \rho c V \frac{dT}{dt} = C \frac{dT}{dt} \tag{20}$$

The heat flow across a boundary between neighboring control volumes is described in terms of a conductance G_{ij} as $Q_{ij} = G_{ij} f(T_i, T_j)$. The functional relationship between the temperatures of the FD points $f(T_i, T_j)$ differs for conduction, radiation, and advection. In summary, the heat balance for the ith control volume is expressed as

$$Q_i + \sum_i G_{ij} f(T_i, T_j) = C_i \frac{dT_i}{dt} \tag{21}$$

B. Accuracy of the IDEAS Software Package

The numerical accuracy of the software package used in the present study is well documented in the heat transfer literature. In the work of Free et al. [17], a comparison of thermal resistance values for pin–fin heat sinks calculated using electronic systems cooling (ESC) software (part of the IDEAS software package) compared with the experimental results of Chapman et al. [18] fall within 10%, with the ESC values being slightly more conservative. In the work of Agonafer and Free [19], comparisons between chip temperature predictions made using an ESC model and the empirical results of Kamath [20], show that the ESC simulations are within 3% of the experimental data. The study of Agonafer and Free [21] documents agreement using ESC for model thermal conduction and convective cooling in an electronics module to be on average, within 10% of agreement with the analytic results of Agonafer and Simons [22]. The investigation of Barrett and Obinelo [23] report numerical ESC results for the thermal performance and flow bypass effects in longitudinal heat sinks which are in very close agreement with the experimental study of Wirtz et al. [24]. The numerical predictions performed by Caldicott and Whalley [25] using TMG to model a forced water cooled heat sink show agreement to within 10% to thermography measurements carried out in the same investigation. More recently in the work of Flowers and Anderson [26], the TMG package was used to model conduction heat transfer in concentric spheres. For additional validation tests, the reader is directed to Flowers and Anderson [26].

VI. Finite Element Thermal Model Results

The temperature prediction for the assembly is shown in Fig. 18. The results indicate a minimum temperature on the order of 243°C (516 K) on the mounting flanges. A maximum temperature of 1360°C (1633 K) occurs in the two-phase flow region of the vaporizer tube/cathode tube annulus. These values correspond to a minimum temperature of 230°C (503 K) over the upper half of the mounting surface of the flange, and a maximum temperature of 1435°C (1708 K) at the end of the vaporizer tube that was calculated

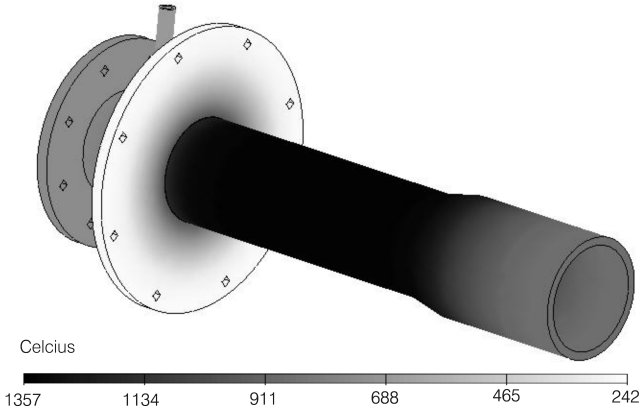

Fig. 18 Temperature contours of the cathode assembly.

using the network model. Overall, the two models show reasonable agreement. This result suggests that the system is not extremely sensitive to the assumptions of neglecting axial heat flow in the channel region and using the simplified radiation views discussed in Sec. II.B. However, because the FETM includes axial heat transfer throughout the cathode, heat lost through conduction to the cold cathode tip is resolved. This has the effect of lowering the temperature at the axial position corresponding to the end of the vaporizer tube. The network model does not capture this effect, thus resulting in higher temperatures at this vaporizer exit.

VII. Conclusions

We have presented a thermal model for the lithium vaporizer based on a resistive network which assumes one-dimensional (radial) heat flow. This model was characterized as first order because it does not include axial conduction back through the structure nor the details of the fluid dynamics (such as pressure drop). Despite these simplifications, the model reveals sensitivity of the vaporizer performance to several design parameters including cathode tube emissivity, mass flow rate, vapor superheat, and number of channels.

Of the parameters we considered, the vaporizer had the greatest sensitivity to the cathode tube emissivity. This is not surprising given that this represents the dominant energy flow path out of the vaporizer in this model. Our results suggest that to the limited extent that emissivity can be controlled in the design (through surface finish, coating, growth of oxide layers, etc.), the emissivity should be as low as tolerable in order to minimize the heater power required for a cold start. Results obtained from the thermal model for the overall thruster, including the arc heat flux, should help in determining the range of allowable values for the emissivity during operation. Another strong driver of vaporizer performance is the heat sunk mounting flange, which caused, in the case modeled, the recondensation of lithium vapor and sudden decreases in the temperature of the cathode assembly (including the fluid). While increasing the thermal resistance to this flange would be favorable (through a thermal choke, insulating ring, etc.), this approach may not be practical, as this mounting flange will need to be able to conduct several thousand amperes of current from the bus bar to the cathode.

The minimum power required to vaporize a fluid between two thermodynamic states scales linearly with mass flow rate. This trend was evident in our results. There are second-order effects as well, since increasing the flow rate will increase the Reynolds number and enhance convective heat transfer. This will have the effect of slightly changing the shape of the vaporizer length–power curves. When we investigated the effect of using multiple channels (between one and six) to vaporize the lithium, we observed the same trend. Fewer channels for the same mass flow rate have the effect of increasing the Reynolds number (and the convective heat transfer) in a given lead/channel, resulting in only minor efficiency gains. These results suggest that the choice of whether to use multiple channels should be based on considerations such as improving uniformity of flow into the plenum or reducing risk of blockage rather than improving thermal efficiency.

We investigated performance sensitivity to the amount of vapor superheat. This parameter is dictated by the need to maintain some margin between the calculated dryout point and the channel exit to the plenum so as to minimize the risk of liquid expulsion or condensation once in the plenum during cold starts. Our baseline case assumed a vapor superheat of 100 K corresponding to a maximum thermal efficiency (the "knee" in the length-power curve) of approximately 59%. At a superheat of 200 K, the efficiency is approximately 55%, but falls to less than 48% at 300 K. This is a direct consequence of the fact the vapor is nearly in thermal equilibrium with the channel walls and there is very little temperature difference to drive the heat flow. Further analysis of flow instabilities which could lead to oscillation of the dryout point along the channel should provide some information as to how much margin is really necessary.

Finally, using the heat flux results of the network model as input, we developed and solved a FETM of the vaporizer/cathode assembly. This model includes all relevant components and heat transfer mechanisms, including radiation boundary conditions and axial conduction (which was neglected in the network model). The FETM results were in reasonable agreement with the results of the resistive network, and are used to further refine the network model.

Acknowledgements

The authors would like to thank both Edgar Choueiri of Princeton University and John Warren of the Prometheus Advanced Systems and Technology Office for support of this work. In addition, Ray Swindlehurst of the Jet Propulsion Laboratory and Andrea Kodys from Princeton University are thanked for their valuable assistance to this paper.

References

[1] Randolph, T., Dougherty, R. C., Oleson, S. R., Fiehler, D., and Dipprey, N., "The Prometheus 1 Spacecraft Preliminary Electric Propulsion System Design," *Proceedings of the 41st AIAA/ASME/ SAE/ASEE Joint Propulsion Conference*; AIAA Paper 2005-3889, July 2005.

[2] Patterson, M. J., Elliot, F., Malone, S. P., Soulas, G. C., Goebel, D., and Sengupta, A., "Herakles Thruster Development for the Prometheus JIMO Mission," *Proceedings of the 41st AIAA/ASME/ SAE/ASEE Joint Propulsion Conference*; AIAA Paper 2005-3890, July 2005.

[3] Frisbee, R., and Moeller, R., "Identification of Mission Sensitivities for High-Power Electric Propulsion Systems," *Proceedings of the 41st AIAA/ASME/ SAE/ASEE Joint Propulsion Conference*; AIAA Paper 2005-3894, July 2005.

[4] Choueiri, E. Y., "Scaling of Thrust in Self-Field Magnetoplasmadynamic Thrusters," *Journal of Propulsion and Power*, Vol. 14, No. 5, Sept/Oct 1998, pp. 744–753.

[5] Kodys, A., and Choueiri, E. Y., "A Review of the State-of-the-Art in the Performance of Applied-Field Magnetoplasmadynamic Thrusters," *Proceedings of the 41st AIAA/ASME/ SAE/ASEE Joint Propulsion Conference*; AIAA Paper 2005-4247, July 2005.

[6] Blandino, J. J., and Goodwin, D. G., "Magnetoplasmadynamic (MPD) Accelerator Assisted Synthesis of Diamond," *Plasma Sources Science and Technology* , Vol. 13, No. 4, 2004, pp. 712–718.

[7] Popov, A., Kim, V., Tikhonov, V., Semenikhin, S., and Tibrina, M., "High-Power Lithium-Fed MPDT Research," The First Quarterly Report on the Items 1 and 2 of Contract No. 960938 Between RIAME MAI and JPL(USA), Technical Report, RIAME MAI, Moscow, June 1998.

[8] Sleicher, C. A., and Rouse, M. W., "A Convenient Correlation for Heat Transfer to Constant and Variable Property Fluids in Turbulent Pipe Flow," *International Journal of Heat and Mass Transfer*, Vol. 18, May 1975, pp. 677–683.

[9] Tong, L. S., and Tang, Y. S., *Boiling Heat Transfer and Two-Phase Flow*, Series in Chemical and Mechanical Engineering, Taylor and Francis, Washington, DC, 1997.

[10] No, H. C., and Kazimi, M. S., "Wall Heat Transfer Coefficients for Condensation and Boiling in Forced Convection of Sodium," *Nuclear Science and Engineering*, Vol. 81, No. 4, 1982, pp. 319–324.

[11] Holman, J. P., *Heat Transfer*, 9th ed., McGraw–Hill, New York, NY, 2002.

[12] Jeppson, D. W., Ballif, J. L., Yuan, W. W., and Chou, B. E., "Lithium Literature Review: Lithium's Properties and Interactions," Hanford Engineering Department Laboratory, HEDL-TME 78-15 UC-20, Richland, WA, 1978.

[13] Yih, S. W. H., and Wang, C. T., *Tungsten: Sources, Metallurgy, Properties, and Applications*, Plenum Press, New York, NY, 1979.

[14] Naraghi, M. H. N., and Chung, B. T. F., "Radiation Configuration Factors Between Disks and a Class of Axisymmetric Bodies," *Journal of Heat Transfer*, Vol. 104, No. 3, August, 1982, pp. 426–431.

[15] Lake, R., *IDEAS TMG Thermal Analysis Master Series User's Guide*, Structural Dynamics Research Corporation, Milford, OH, 2000.

[16] Lake, R., *IDEAS-TMG User's Guide*, Maya Heat Transfer Technologies, Montreal Canada, 1996.

[17] Free, J. A., Russell, R., and Louie, J., "Recent Advances in Thermal and Flow Simulation: Integrating Thermal Analysis into the Mechanical Design Process," *11th IEEE Semi-Therm Conference*, 1995.

[18] Chapman, C., Lee, S., and Schmidt, B., "Thermal Performance of an Elliptical Pin Fin Heat Sink," *Proceedings of the 10th Semiconductor Thermal and Temperature Measurement Symposium*, IEEE Press, New York, Feb. 1994, pp. 24–31.

[19] Agonafer, D., and Free, J. A., "Conjugate Model of a Pin-Fin Heat Sink Using a Hybrid Conductance and CFD model Within an Integrated MCAE Tool," presented at *Eurotherm Seminar No. 45*, Sept. 1995.

[20] Kamath, V., "Air Injection and Forced Convection Cooling of Single and Multi-Chip Modules: A Computational Study," *Proceedings of the 14th ITHERM Conference*, IEEE Catalog No. 94CH3340-7, pp. 83–90.

[21] Agonafer, D., and Free, J. A., "Numerical Modeling of an Entire Thermal Conduction Module Using a Thermal Coupling Methodology," *ASME International Mechanical Engineering Congress*, 1995.

[22] Agonafer, D., and Simons, R. E., "Optimization Trade-Off Analysis on a Thermal Conduction Module Package Using CAEDS," *Proceedings of ASME HTD, ASME/AIAA Joint Thermophysics Conference*, ASME, Boston, New York, 1995.

[23] Barrett, A. V., and Obinelo, I. F., "Characterization of Longitudinal Fin Heat Sink Thermal Performance and Flow Bypass Effects Through CFD Models," *SEMITHERM 3*, IEEE, Washington, DC, 1997.

[24] Wirtz, R. A., Chen, W., and Zhou, R., "Effect of Flow Bypass on the Performance of Longitudinal Fin Heat Sinks," *Journal of Electronic Packaging*, Vol. 116, No. 4, 1994, pp. 206–211.

[25] Caldicott, A. S., and Whalley, D. C., "Design Analysis of a Forced Water Cooled Heatsink," EEP Vol. 19-2, *Advances in Electronic Packaging*, American Society of Mechanical Engineers, New York, NY, 1997.

[26] Flowers, D., and Anderson, K., "Numerical Simulation of Conduction Heat Transfer in a System of Slowly Rotating Concentric Shells Separated by Small Annular Gap Distances," *Numerical Heat Transfer, Part A, Applications*, Vol. 46, No. 9, 2004, pp. 851–867.

R. Myers
Associate Editor